Image Reconstruction of Targets in Random Media from Continuous Wave Laser Measurements and Simulated Data

J. Chang, H. L. Graber, and R. L. Barbour
State University of New York, Health Science Center at Brooklyn, 450 Clarkson Avenue, Brooklyn, New York 11203

J. Chang and R. L. Barbour are with the Department of Pathology.
H. L. Graber and R. L. Barbour are with the Department of Biophysics.

Abstract

Four algorithms - POCS, CGD, SART and a SART-type method with regularization, were used to reconstruct images of targets in dense scattering media. The convergence rates and image quality are evaluated.

1. Introduction

Efforts to image the interior properties of tissues at near-infrared frequencies seem to be evolving along two distinct tracks. One approach, taken by many, is to acquire 2-dimensional projection images of a test medium based on diffuse transmission or backscatter measurements, typically performed using time-resolved or amplitude-modulated sources. The advantage of this scheme is that inferences about tissue structure and properties are obtained directly without the need for any significant computational effort. As with x-ray imaging, the quality of these images will depend strongly on detection of a straight-line or nearly straight-line signal. For most structures of clinical interest (*e.g.*, breast, limbs, head, and trunk) however, the optical thicknesses are sufficiently large to cause the intensity of these signals to become vanishingly small. Under these conditions, image recovery will be strictly dependent on evaluation of highly scattered photons, regardless of the measurement technique employed. Our approach to imaging the interior of tissues using optical sources explicitly considers solution of the 3-dimensional inverse scattering problem, using perturbation methods derived from the transport equation. Because detected photons have propagated though relatively large volumes, these methods are unavoidably computationally intensive. In prior studies [1-3], we have evaluated the inverse problem using simulated data derived from various target media. More recently [4, 5], we have experimentally validated the perturbation approach using model media having optical dimensions of clinical interest. In this study, we have extended these analyses and compare four reconstruction algorithms - POCS [6], CGD [7], SART [8] and a SART-type [4] method, with regularization [9]. The convergence rate and image quality were evaluated for 1-D, 2-D and 3-D image reconstructions using the different reconstruction algorithms.

2. Perturbation Model

The perturbation model [1-5] adopted for optical diffusion tomography relates the differences between the absorption properties of target and reference media, $\Delta x_j = x_j - x_j^r$, to changes in detector readings, $\Delta I_i = I_i - I_i^r$, by the following first order approximation:

$$\sum_j w_{ij} \Delta x_j = \Delta I_i, i = 1, 2, \ldots, K. \quad (1)$$

Here, K is the total number of source-detector pairs, and w_{ij} is called the *weight*, which is proportional to the product of collision densities due to photons propagating from the source to voxel j and from the detector to voxel j. The above linear equation can be represented in matrix form as:

$$\mathbf{W}\Delta\mathbf{x} = \Delta\mathbf{I}. \quad (2)$$

OSA Proceedings on Advances in Optical Imaging and Photon Migration, 1994, Vol. 21, R. R. Alfano (ed.)

3. Simulation and Experiment

Numerical and experimental studies were performed to examine the ability to reconstruct the interior properties of dense scattering media by analyzing surface measurements.

Numerical studies (Figure 1) modeled 3-D nonabsorbing isotropically scattering media having cylindrical geometry and a diameter of 20 mean free pathlengths (mfp), using Monte Carlo methods, from which surface detector readings and imaging operators were computed. The latter, referred to as weight functions, were derived from the product of computed direct and adjoint collision densities [1, 4]. Surface detector readings were computed for two types of media. One contained a single black rod having a diameter of 2 mfp, placed in a centered or off-center position. The other contained 13 black rods, each having a diameter of 0.5 mfp, oriented in a "X", *i.e.*, cross, pattern. The sources were incident at different angles surrounding the phantom and the detectors were located at 36 different locations (10° separation) for each source (Figure 2). The readings were normalized according to number of incident photons.

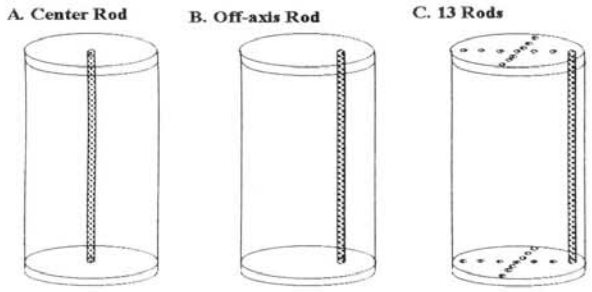

Figure 1. Tissue phantoms used for Monte Carlo simulations.

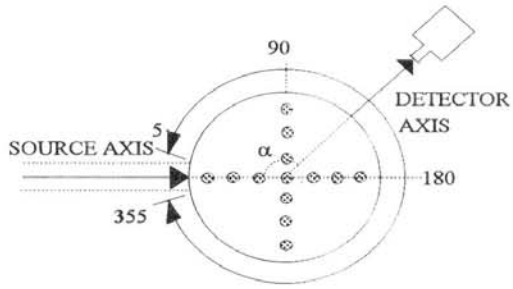

Figure 2. Simulation source and detector configuration.

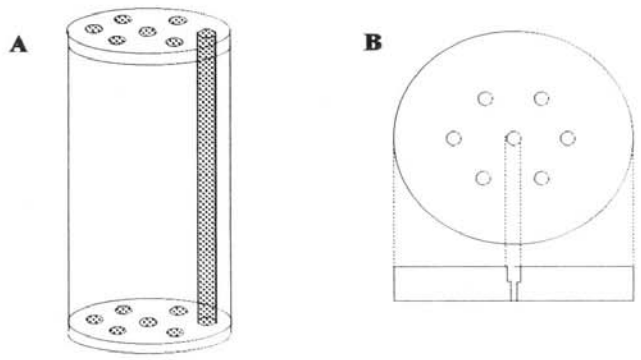

Figure 3. Tissue phantom used for experiments.

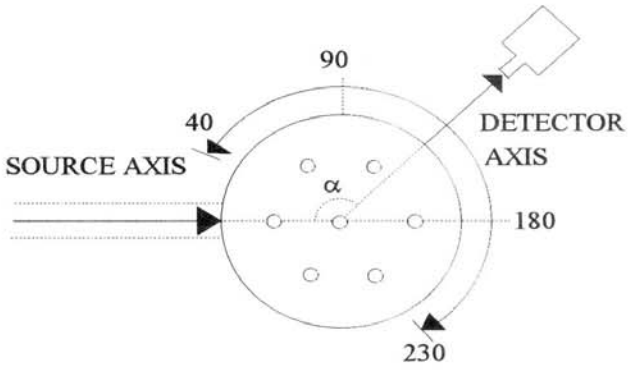

Figure 4. Experimental source and detector configuration.

Figure 3A shows a sketch of the tissue phantom and Figure 3B shows the face- and edge-on views of the disk that anchors the absorbing rods at the bottom. An 8 cm (dia.) cylinder was filled to a height of 35 cm with a suspension of Intralipid® fat emulsion diluted with water. Three sets of measurements were performed, with suspensions containing 2%, 0.4%, and 0.08% lipid by volume. A 2% solution was prepared by performing a 1:5 dilution of the commercially available 10% stock solution. The transport-corrected scattering length for the 2% medium at 720 nm was estimated as being 0.3-0.5 mm. One rod was inserted into the cylinder as a heterogeneity. Two experiments were performed - one with a rod at the center, and the other with a rod half-way between the center and boundary. The sources were incident at 6 different angles around the phantom and the detectors were located at 20 different locations (10° separation in angle) for each source (Figure 4). The readings were normalized according to the lens aperture, exposure time, camera gain, and intensity of the laser source. The differences between the reference and target media

readings were then calculated for image reconstruction.

4. Reconstruction Algorithms

Four iterative algorithms - (1) projection onto convex sets (POCS) [6], (2) conjugate gradient descent (CGD) [7], (3) simultaneous algebraic reconstruction algorithm (SART) [8], and (4) a SART-type algorithm [4], all based on the perturbation model Eq. 1, were used for image reconstruction.

POCS is a sequential projection method which reaches the intersection point of L constraint sets by projecting the current estimate of the solution onto each set C_l (a set which satisfies the l^{th} constraint), $l = 1,2, \ldots, L$, sequentially and iteratively. Letting $\Delta\mathbf{x}^n$ represent the estimate at the n^{th} iteration, each step in POCS can be represented by:

$$\Delta\mathbf{x}^{n+1} = \mathrm{P_L} \circ \mathrm{P_{L-1}} \circ \ldots \mathrm{P_1}\, \Delta\mathbf{x}^n . \tag{3}$$

Here, P_l represents the projection operator onto C_l, such that $\mathrm{P}_l\, \Delta\mathbf{x}^n$ is the element in C_l that is closest to $\Delta\mathbf{x}^n$. Youla [2] has proved that, as long as the intersection of the constraint sets is not empty, iterative projections onto these sets will converge to their intersection.

The CGD update was computed according to the conjugate gradient direction **d**:

$$\begin{aligned} \mathbf{g}^n &= \frac{\partial E}{\partial \Delta\mathbf{x}} = \mathbf{W}^{\mathrm{T}}\mathbf{C}(\Delta\mathrm{I}^n - \Delta\mathrm{I}), \\ \mathbf{d}^n &= g^n + \beta\mathbf{d}^{n-1},\ \Delta\mathbf{x}^{n+1} = \Delta\mathbf{x}^n - \alpha\mathbf{d}^n, \end{aligned} \tag{4}$$

where E is the mean squared error, and α is called the step-size, which must be chosen appropriately to guarantee convergence. Theoretically, this algorithm should converge after a number of iterations less than or equal to the number of unknowns.

The SART algorithm updates the reconstruction as follows:

$$\Delta x_j^{n+1} = \Delta x_j^n + \frac{\sum_i w_{ij} \cdot \dfrac{\Delta I_i - \sum_j w_{ij} \cdot \Delta x_j^n}{\sum_j w_{ij}}}{\sum_i w_{ij}} . \tag{5}$$

The SART-type algorithm is similar to SART algorithm with minor modification:

$$\Delta x_j^{n+1} = \Delta x_j^n + \frac{\sum_i w_{ij} \left[\left(\dfrac{\Delta I_i}{I_i^r} \right) - \dfrac{\sum_j w_{ij} \cdot \Delta x_j^n}{\sum_j w_{ij}} \right]}{\sum_i w_{ij}} . \tag{6}$$

Different combinations of regularization constraints were used [9]: (1) unconstrained, (2) positivity constraint on reconstruction results, (3) positivity constraints on detector readings and reconstruction results. Range constraints on detector readings were imposed prior to reconstruction, with all the negative readings set to zero. The range constraints on reconstruction results were imposed after each iteration.

The convergence rate and image quality were evaluated for each combination of algorithm and constraints. For the experimental data, 1-dimensional reconstructions (forcing the image to be symmetric both radially and along the axis) in the centered rod case, and 2-dimensional reconstructions (symmetry in direction parallel to axis imposed on image) were performed using CGD, POCS, and SART-type algorithm. For simulation data, 2- and 3-dimensional reconstructions (no imposition of symmetry) were performed using all four methods. Only 1-D and 2-D reconstruction results are reported here.

5. Results

Figure 5 shows a cross-sectional cut of the voxel geometry used for this study. Classical cylindrical

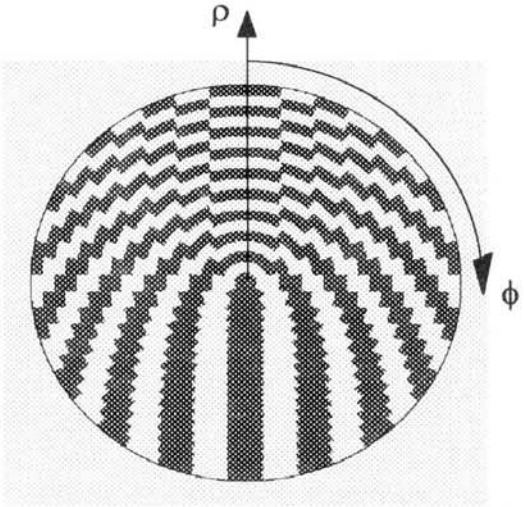

Figure 5. Illustration of voxel geometry and cylindrical coordinate system used in this study. The z-direction is normal to the surface of the page.

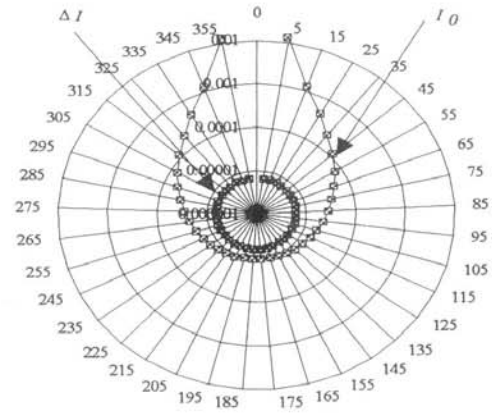

Figure 6. Monte Carlo simulation results of log of absolute intensities (I_0) and difference intensities ($\Delta I = I_0 - I$).

coordinates were used and the whole 3-D volume was discretized into 16,000 voxels bounded by surfaces of constant ρ, ϕ and z, with each voxel having the same volume. Figure 6 shows a plot of the log of computed absolute detected intensities and intensity differences, for the centered rod simulation. It can be seen that the absolute intensities range over more than 3 order of magnitude, while the differences are almost constant for all values of the angle ϕ, which is consistent with the prediction of the perturbation model.

Figure 7 shows the reconstruction result for the case of a centered rod from simulated data. This case was selected for study because it is the central region of a medium that is most difficult to resolve. Inspection reveals that the SART and SART-type algorithms produced a nearly perfect reconstruction. A good quality image was also obtained using POCS, while the CGD result contained numerous artifacts farther from the center. Figure 8 demonstrates the results for the case when the rod is located off-center. SART and POCS accurately located the absorber, with minimal artifacts, while SART-type method underestimates the distance of the rod from the center by 2-3 voxels. Similar to the results shown in Figure 7, results from the CGD method produced significant artifacts. This observation is not completely unexpected, as no constraints were imposed during the reconstruction. Overall, these data clearly show that analysis of time-independent data using a perturbation model is capable of resolving the internal structure of a dense scattering medium.

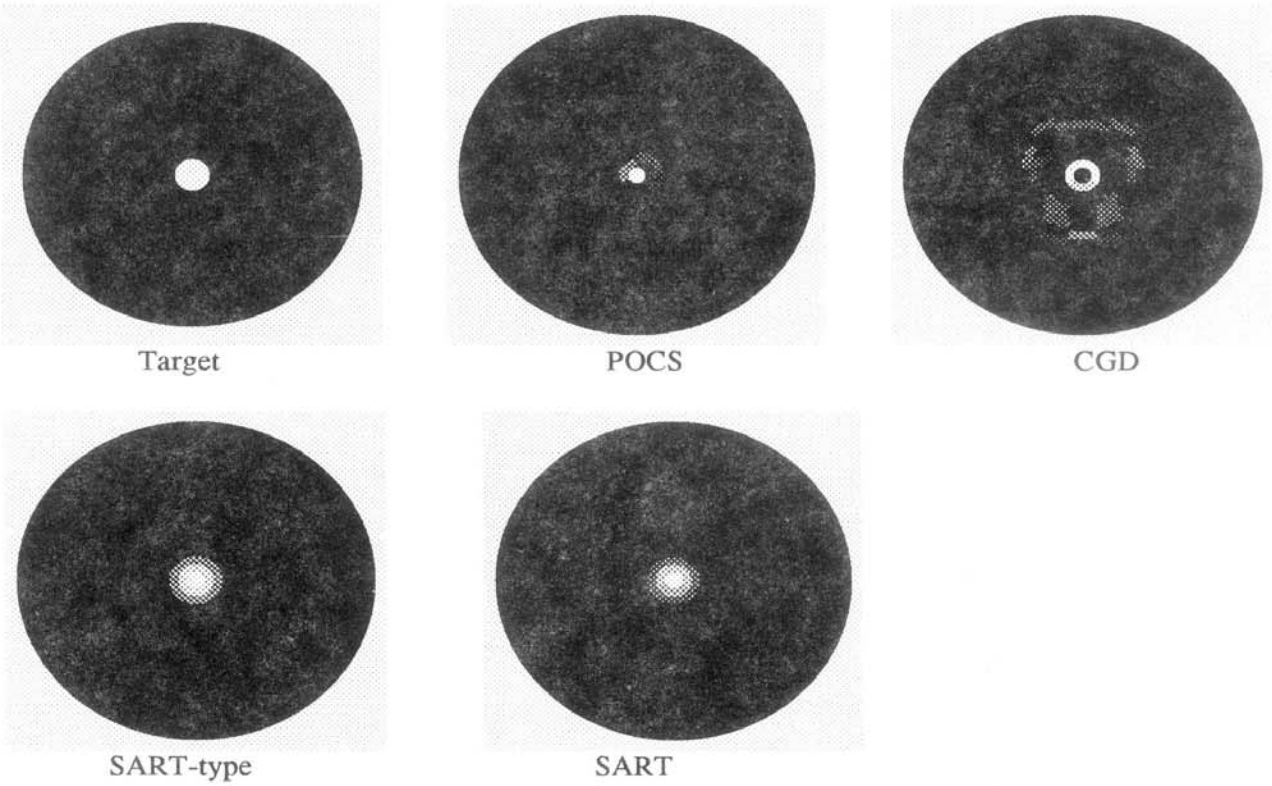

Figure 7. 2-D reconstructed images of centered rod case from simulation data after 10,000 iterations. "Target" is the medium from which ΔI was generated.

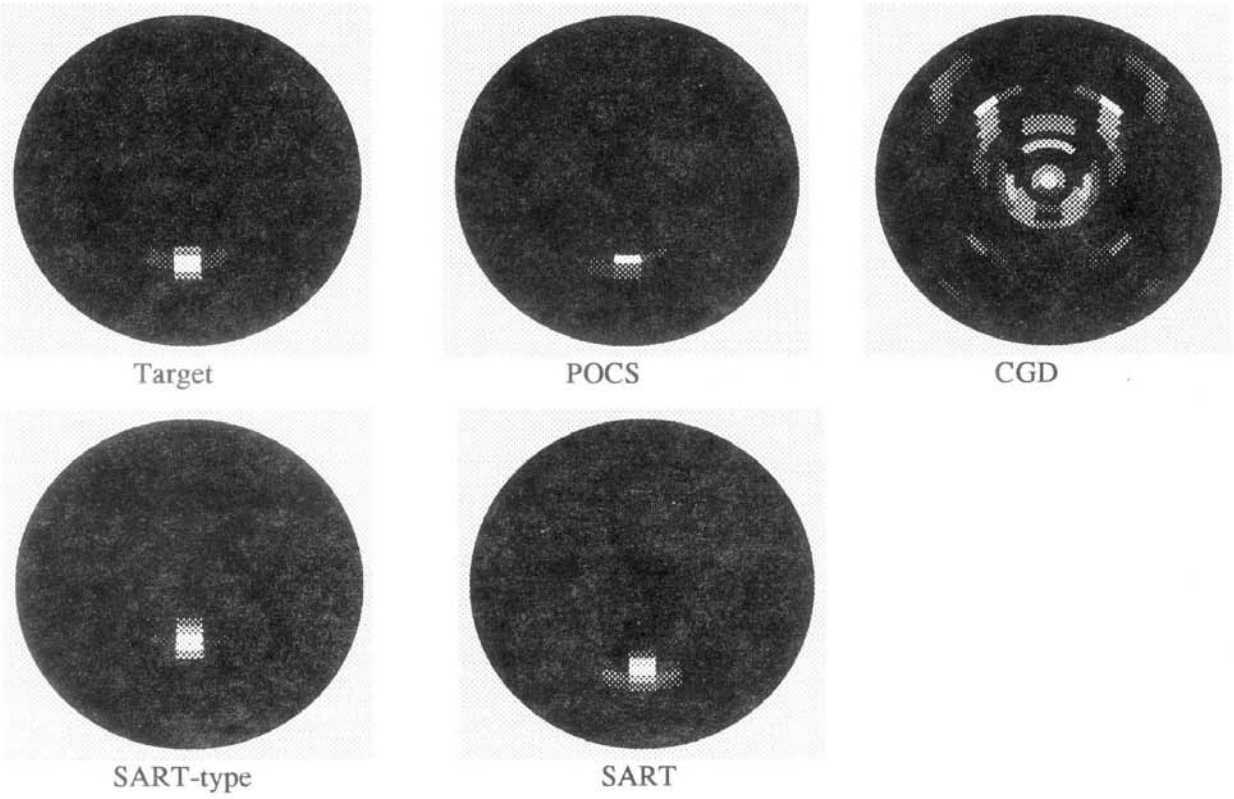

Figure 8. 2-D reconstruction results of the off-center rod case from simulation data after 100,000 iterations. "Target" is the medium from which ΔI was generated.

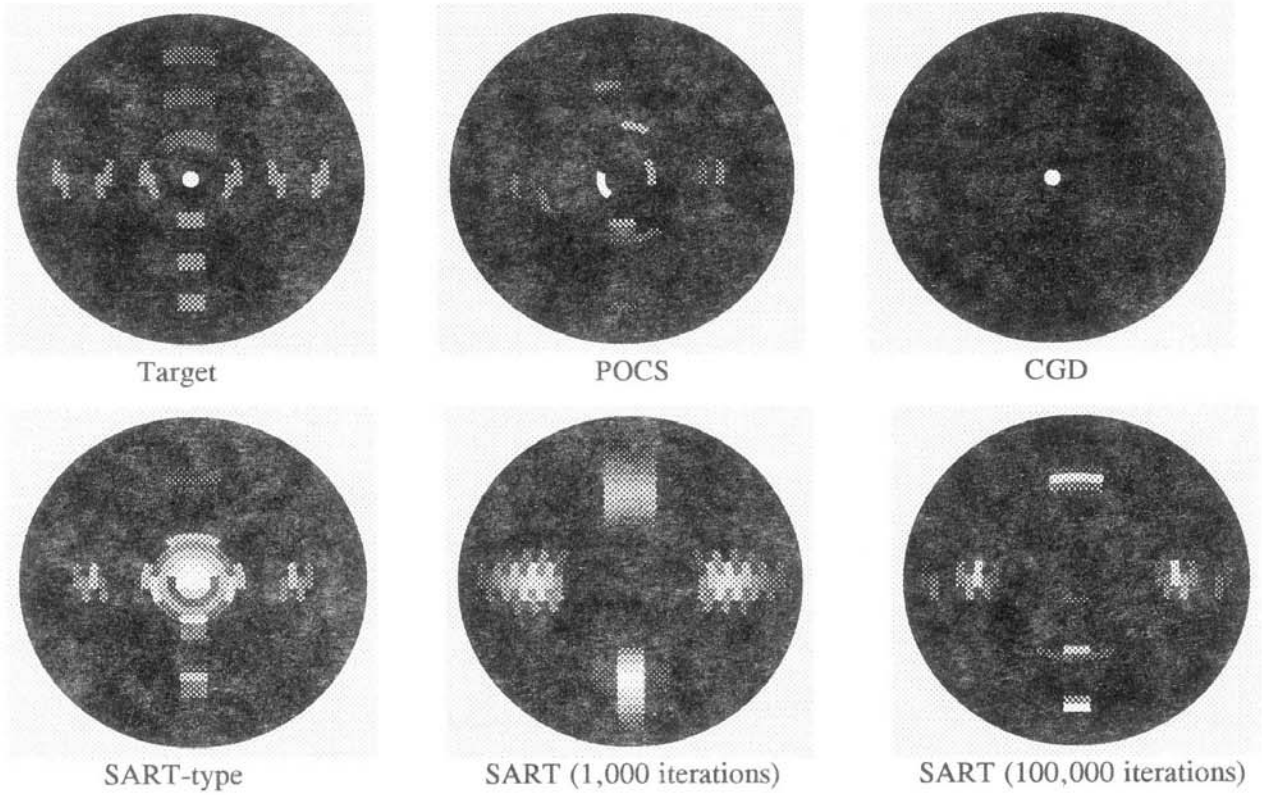

Figure 9. 2-D reconstructed images of 13 rod case from simulation data after 10,000 iterations for POCS, CGD, and SART-type method, and after 1,000 and 100,000 iterations for SART. "Target" is the medium from which ΔI was generated.

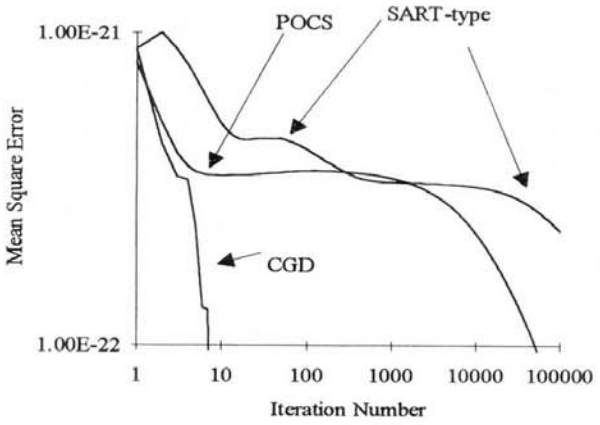

Figure 10. Mean squared error *vs.* iteration for different algorithms.

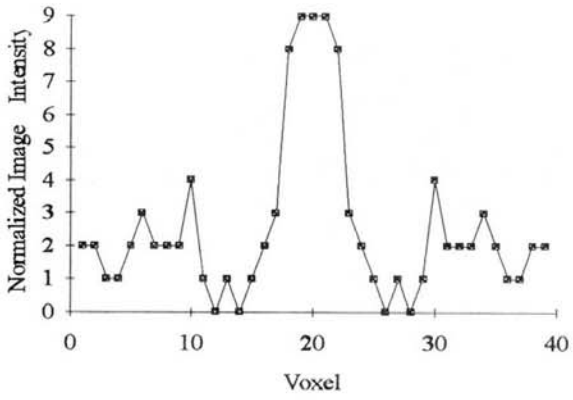

Figure 11A. Unconstrained reconstructed image using the SART-type algorithm.

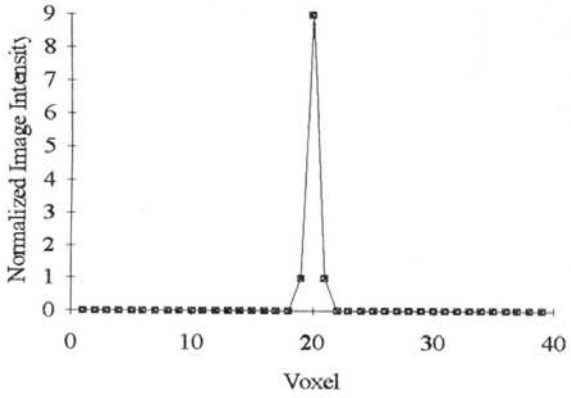

Figure 11B. Reconstructed image using the SART-type algorithm, with positivity constraints imposed on both detector readings and reconstructed results.

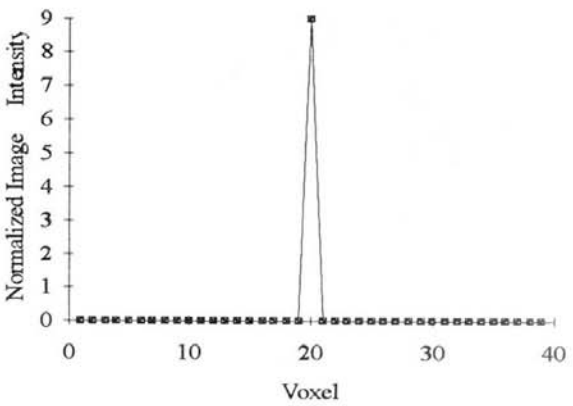

Figure 11C. Image of the target medium from which ΔI was generated.

Further tests of the accuracy of the perturbation model conducted using a medium containing a complex internal structure are shown in Figure 9. While in all cases the image quality was less than that observed for the single rod example, identification of the general structure of the medium is unmistakable. The trend in image quality followed the inequality observed in the previous test cases, *i.e.*, SART > SART-type > POCS > CGD. The apparent failure of the SART algorithm to accurately resolve the central features of the medium we believe is due to the significant overestimation of weight in this region due to the presence of the absorbing rods. Interestingly, the SART-type algorithm seemingly exhibited greater sensitivity to the central region.

Figure 10 shows the mean squared error $|\Delta \mathbf{I}'' - \Delta \mathbf{I}|^2$ of three of the four iterative algorithms for 1-dimensional unconstrained image reconstruction in the centered rod case during the first 10,000 iterations. As expected, CGD converges much faster (under 1,000 iterations) than the other algorithms.

Figure 11 shows the reconstructed image derived from experimental data for the case when the absorbing rod is located in the center of the vessel using the SART-type algorithm. The unconstrained result is shown in Panel A, the constrained result (positivity constraints on both detector readings and reconstruction results), is shown in Panel B and the target medium from which ΔI was generated is shown in Panel C. Inspection of Panel B reveals that a nearly perfect reconstruction was obtained. We consider this finding very significant, as these measurements were performed with a medium having an optical thickness equivalent to a large uncompressed female breast. The observed strong dependence of image quality on use of constraints

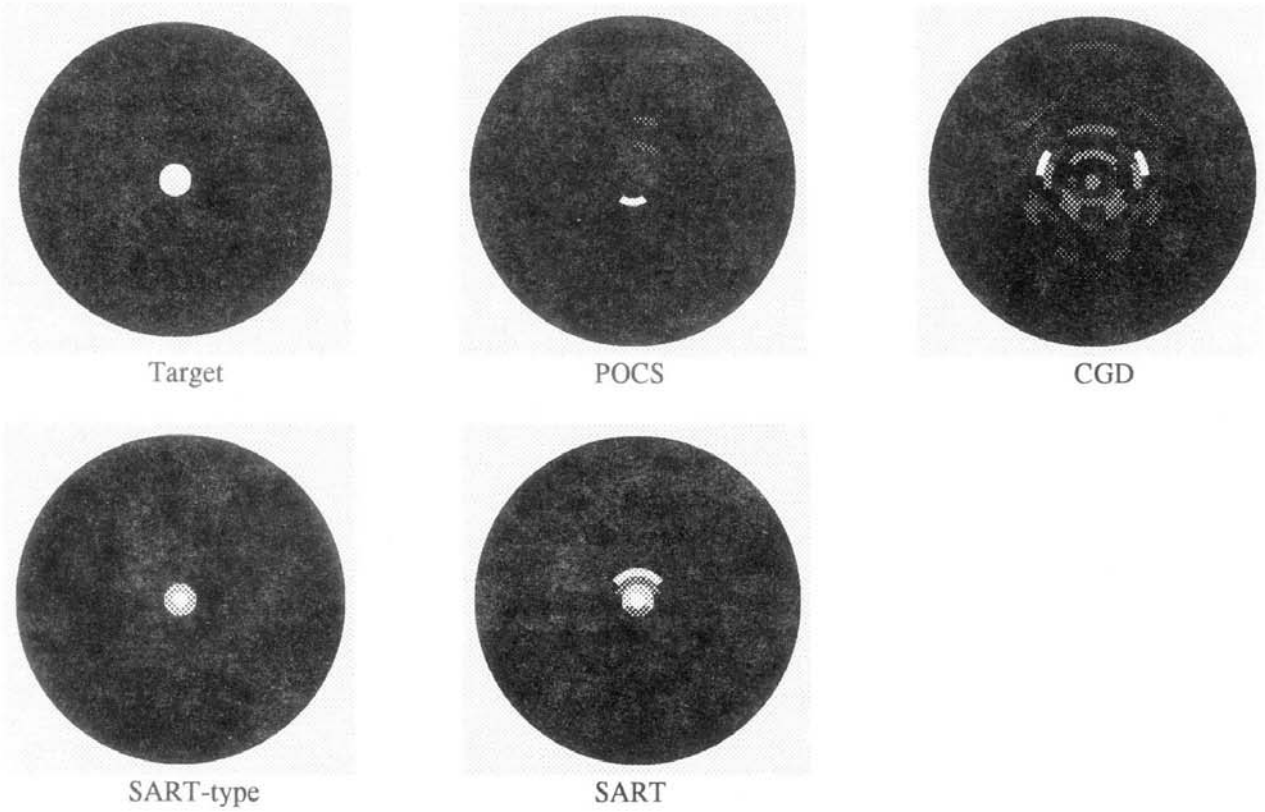

Figure 12. 2-D reconstructed results of centered rod case from experimental data after 10,000 iterations. "Target" is the medium from which ΔI was generated.

underscores the need to constrain the solution space. The imposition of constraints, however, causes all of the algorithms tested to converge more slowly. We also observed that the SART-type algorithm had a higher mean squared error than CGD and POCS.

Figure 12 shows the 2-D reconstruction results for the centered rod case from experimental data. Similar to the results from simulated data, the SART and SART-type algorithm produced the best results. Overall, the reconstruction results for the experimental data contained a greater level of artifacts. This finding is not surprising due to the higher noise levels in the experimental data. Results shown in Figure 13 illustrate the image quality obtained from experimental data with the absorbing rod located in an off-center position. Inspection reveals that the CGD algorithm in this case produced the most accurate location of the absorber, but contained artifacts at the boundary. The SART-type algorithm result was much less noisy, but the absorber position incorrectly located too close to the center by a small amount.

6. Conclusions

Results reported here directly demonstrate that sufficient information exists in measured data at the boundary of a dense scattering medium to permit an accurate reconstruction of simply structured media having dimensions of clinical interest. Extrapolation of these results to evaluate different body structures will depend on the assumed transport mean free path length of the tissue. Assuming a transport–corrected scattering cross section of 1 mm^{-1}, the experimental finding here would suggest that it may be possible to accurately image even large diameter breasts.

In these studies we have evaluated the ability to image the presence of one or more black rods in a dense scattering medium. It is important to recognize that while these conditions will enhance the detector response, they introduce significant errors in modeling. This follows since the perturbation model is most accurate in the presence of a small perturbation. Thus there is a tradeoff between improved detector response caused by greater contrast and the possible modeling errors introduced by strong discontinuities. One approach to reduce the modeling errors would be to base the derived imaging operators on a medium whose internal structure and contrast is similar to that being investigated. Recently we have begun to explore use of MRI data from which can be

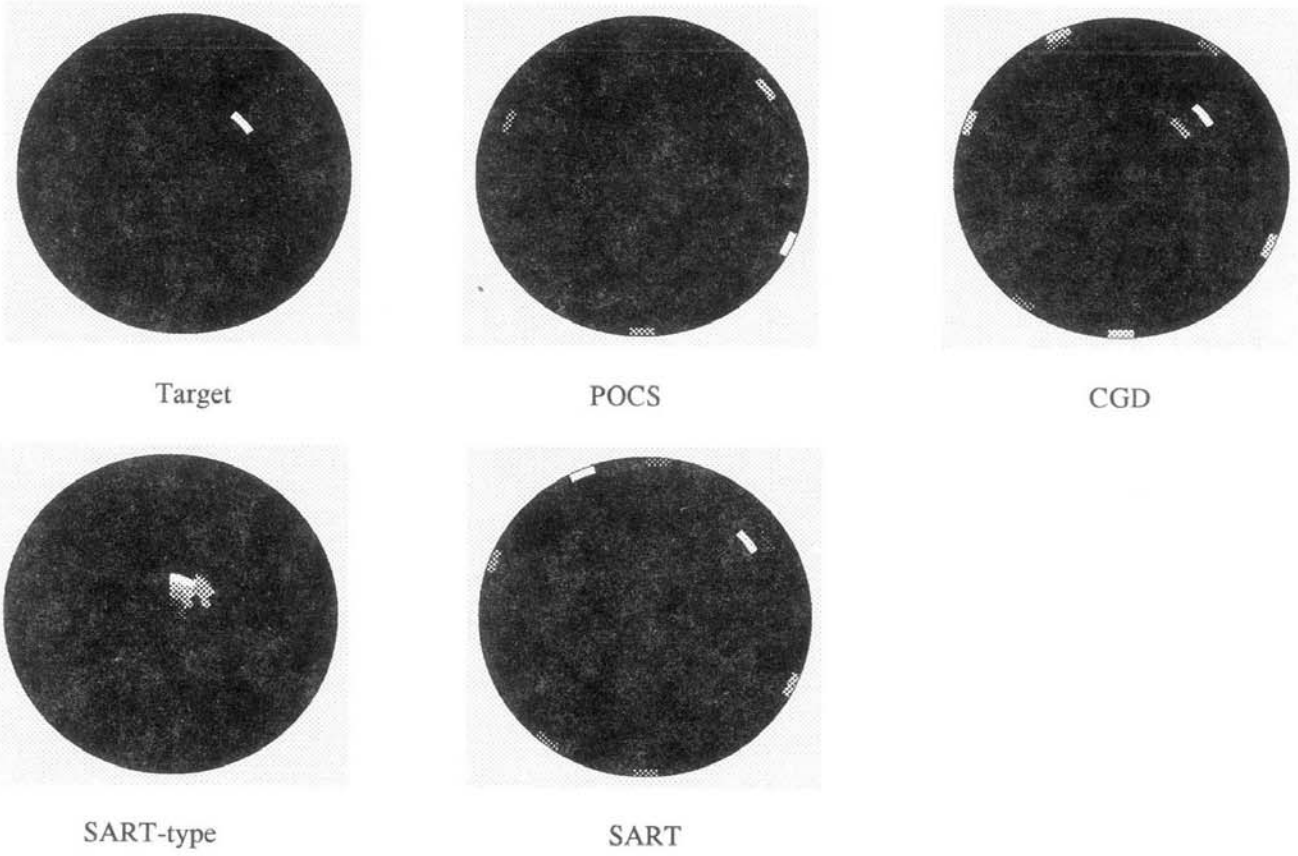

Figure 13. 2-D reconstructed results of off-centered rod case from experimental data after 10,000 iterations. "Target" is the medium from which ΔI was generated.

derived anatomically accurate optical reference maps. An additional appeal of this approach is the prospect of simultaneously obtaining an optical measurement during an MRI scan. In this case the body tissue being probe could also act as the reference medium.

7. Acknowledgment

This work was supported in part by NIH grant R01 CA59955 and by the New York State Science and Technology Foundation.

8. References

1. R. L. Barbour, H. L. Graber, R. Aronson and J. Lubowsky, "Imaging of subsurface regions of random media by remote sensing," SPIE vol. 1431, 192-203 (1991).
2. R. L. Barbour, H. L. Graber, J. Lubowsky, R. Aronson, B. B. Das, K. M. Yoo and R. R. Alfano, "Imaging of diffusing media by a progressive iterative backprojection method using time-domain data," SPIE vol. 1641, 21-34 (1992).
3. Y. Wang, J. Chang, R. Aronson, R.L. Barbour, H. L. Graber and J. Lubowsky, "Imaging of scattering media by diffusion tomography: An iterative perturbation approach," SPIE vol. 1641, 58-71 (1992).
4. H.L. Graber, J. Chang, R. Aronson, R.L. Barbour, "A Perturbation Model for Imaging in Dense Scattering Media: Derivation and Evaluation of Imaging Operators", in Medical Optical Tomography: Functional Imaging and Monitoring, (SPIE Press, 1993) SPIE Institutes vol. IS11, pp. 121-143.
5. H. L. Graber, J. Chang, J. Lubowsky, R. Aronson and R.L. Barbour, "Near infrared absorption imaging of dense scattering media by steady-state diffusion tomography," SPIE vol. 1888, 372-386 (1993).
6. D.C. Youla, "Mathematical Theory of Image Reconstruction," Image Recovery: Theory and Application, Henry Stark, ed. (Academic Press, 1987).
7. P.E. Gill, W. Murray, and M.H. Wright, Practical Optimization (Academic Press, 1981).

8. A.V. Kak and M. Slaney, Principles of Computerized Tomographic Imaging (IEEE Press, 1988).
9. G.A. Deschamps and H.S. Garayan, "Antenna Synthesis and Solution of Inverse Problems by Regularization Methods," *IEEE Trans. Antennas Propagat.*, AP 20, 268-274 (1972).